

A Dendritic Nickel Cobalt Sulfide Nanostructure for Alkaline Battery Electrodes

Wenyao Li, Bingjie Zhang, Runjia Lin, SocMan Ho-Kimura, Guanjie He,* Xiying Zhou, Junqing Hu,* and Ivan P. Parkin*

A uniform dendritic $\text{NiCo}_2\text{S}_4@ \text{NiCo}_2\text{S}_4$ hierarchical nanostructure of width ≈ 100 nm is successfully designed and synthesized. From kinetic analysis of the electrochemical reactions, those electrodes function in rechargeable alkaline batteries (RABs). The dendritic structure exhibited by the electrodes has a high discharge-specific capacity of 4.43 mAh cm^{-2} at a high current density of 240 mA cm^{-2} with a good rate capability of 70.1% after increasing the current densities from 40 to 240 mA cm^{-2} . At low scan rate of 0.5 mV s^{-1} in cyclic voltammetry test, the semidiffusion controlled electrochemical reaction contributes $\approx 92\%$ of the total capacity, this value decreases to $\approx 43\%$ at a high scan rate of 20 mV s^{-1} . These results enable a detailed analysis of the reaction mechanism for RABs and suggest design concepts for new electrode materials.

1. Introduction

With the increasing demand for sustainable and renewable energy resources, electrical energy storage technologies are becoming


Prof. W. Y. Li, Prof. X. Y. Zhou
School of Materials Engineering
Shanghai University of Engineering Science
Shanghai 201620, China

Prof. W. Y. Li, Prof. X. Y. Zhou
Shanghai Innovation Institute for Materials
Shanghai 200444, China

Dr. B. J. Zhang, Prof. J. Q. Hu
State Key Laboratory for Modification of Chemical
Fibers and Polymer Materials
College of Materials Science and Engineering
Donghua University
Shanghai 201620, China
E-mail: hu.junqing@dhu.edu.cn

R. J. Lin, Dr. G. J. He, Prof. I. P. Parkin
Materials Chemistry Centre
Department of Chemistry
University College London
20 Gordon Street, London WC1H 0AJ, UK
E-mail: guanjie.he.14@ucl.ac.uk; i.p.parkin@ucl.ac.uk

Dr. S. Ho-Kimura
Institute of Applied Physics and Materials Engineering
University of Macau
Avenida da Universidade
Taipa, Macau SAR, China

 The ORCID identification number(s) for the author(s) of this article can be found under <https://doi.org/10.1002/adfm.201705937>.

© 2018 The Authors. Published by WILEY-VCH Verlag GmbH & Co. KGaA, Weinheim. This is an open access article under the terms of the Creative Commons Attribution License, which permits use, distribution and reproduction in any medium, provided the original work is properly cited.

DOI: 10.1002/adfm.201705937

more important for green vehicles and portable devices.^[1] Supercapacitors and lithium-ion batteries (LIBs) are at the forefront of energy storage system are widely studied.^[2] Supercapacitors have attracted intense interest and wide ranging applications since they can provide superb power densities and long cycle life.^[3] However, supercapacitors suffer from relatively low energy densities and low capacitance due to the mechanism of surface electrochemical storage between the electrolyte and the active materials.^[4] LIBs, on the other hand, can provide higher energy density, but are problematic due to their relatively low power

densities. In certain situations, energy storage devices need to exhibit both relatively higher energy density compared to supercapacitors and higher power density compared to LIBs. Therefore, a novel hybrid energy storage system—rechargeable alkaline batteries (RABs)—has been defined and considered as a promising device.^[5] In RABs, the electrochemical reactions mainly happen within the bulk electrodes in aqueous electrolytes.

Recently, nickel cobalt-based nanostructures have attracted intensive interest in various electrochemical applications, such as LIBs^[5a] and RABs,^[5b] owing to their abundance in nature, high capacity, and good reversibility.^[6] NiCo_2S_4 has exhibited outstanding performance compared to other nickel cobalt-based systems.^[7] On one hand, the electrical conductivity of NiCo_2S_4 is at least two times higher than that of NiCo_2O_4 due to their smaller band gap.^[8a] On the other hand, NiCo_2S_4 has exhibited higher electrochemical activity and higher capacity than other single-metal oxides or sulfides due to their inherent redox reaction centers.^[8b] In some previous work, various 3D structures, such as nanoflowers,^[9] core-shell structures,^[10] and dendritic structure^[11] have been designed and synthesized. For example, Xia and co-workers have synthesized NiCo_2S_4 urchin-like nanostructure through a facile precursor transformation method, these materials have shown a capacity retention of 77.3% when the current density was increased 20 times from 1 to 20 A g^{-1} in an aqueous electrolyte. Also, a specific capacity retention of 91.4% has been observed after 5000 cycles at a high current density of 20 A g^{-1} .^[12] Wang and co-workers have reported the synthesis of NiCo_2S_4 by a simple one-step hydrothermal approach. Their material exhibited a capacitance retention of 53.2% when the current density increased from 1 to 20 A g^{-1} . Moreover, after 1000 cycles at a fixed current density of 20 A g^{-1} , a retention of 81% in specific capacitance was achieved.^[4] Despite the progress in the energy storage properties of the nickel cobalt-based system that has been achieved, the increase of the areal-specific capacity,

rate performances, and cycling stability of these materials still remain as challenges.^[5] One effective way to improve the rate capacity of NiCo₂S₄ materials is to develop hierarchical heterostructures since these 3D interconnected networks and porous structures can provide larger surface areas and thus larger contact area for the electrolyte, which can accelerate the efficient charge and mass exchange during Faradic redox reactions.^[10]

In this work, we have designed a new hierarchical structure of dendritic NiCo₂S₄@NiCo₂S₄ nanoarrays by a three-step continuous hydrothermal process with the aim to optimize the electrochemical performances of Ni-Co-S system. This approaches sufficient pathways for immersing the electrolyte to enable efficient charge and mass transfer within the bulk materials. The active materials were integrated on current collectors as self-standing electrodes, this route avoids the complicated electrodes fabrication procedure compared with slurry-making powdery materials.^[13] This specific structure showed large areal-specific capacity, high rate capability, and excellent stability as electrodes for RABs.

2. Results and Discussion

The whole fabrication procedure for dendritic NiCo₂S₄@NiCo₂S₄ hierarchical heterostructures is schematically presented in Figure 1a. A facile hydrothermal route followed by a calcination process resulted in a high density of NiCo₂O₄ porous nanorod arrays grown vertically on a Ni foam; after that, a thin layer of NiCo₂O₄ nanosheets was coated on the as-grown NiCo₂O₄ porous nanorod arrays by a controllable hydrothermal route; finally, the S²⁻ exchange process induced the growth of dendritic NiCo₂S₄@NiCo₂S₄ hierarchical heterostructures (details are provided in the Experimental Section). In step I, the nanostructure morphology is closely related to the ligand environment of the cation, the Co²⁺ and Ni²⁺ cations are hexacoordinate with urea. Furthermore, the Co²⁺ and Ni²⁺ cations reacted with the hydrolysis products of urea (CO₃²⁻ and OH⁻) to form bimetallic carbonate hydroxide precursors.^[14] After annealing, porous NiCo₂O₄ formed along with the evaporation of H₂O (g) and CO₂. In step II, the existence of mutual stresses from the defects on the surface of the porous structure of NiCo₂O₄, caused overlapping and rolling of the materials in different directions, in addition, the Co²⁺ and Ni²⁺ cations with hexamethylenetetramine (HMT) are typically tetraordinated. These two factors seem to lead the nanosheets to form nanoblocks along the vertical and horizontal directions via bridging. In step III, the open structure of nanosheets and porous NiCo₂O₄ promoted the diffusion of sulfur sources into the core of the nanorods, thus converting the NiCo₂O₄ to homogenous NiCo₂S₄.^[15] Interestingly, because of the bigger ionic radius of S²⁻ (0.18 nm) compared to O²⁻ (0.14 nm), mesoporous structures could be formed due to the replacement of O²⁻ by S²⁻ through the sulfurization process.^[16] Down to the atomistic scale in Figure 1b,c, the low index facets of NiCo₂S₄ are (111) and (100). The maximum geometry diameter of them showed the same value of ≈0.66 nm, while the minimum geometry diameter can be measured as ≈0.41 and ≈0.39 nm for (111) and (100), respectively. These results delivered the possibility of large and open channels for the diffusion of OH⁻ ions (kinetic diameter of H₂O is ≈0.27 nm) from surface to the bulk of NiCo₂S₄, thus providing the prerequisite

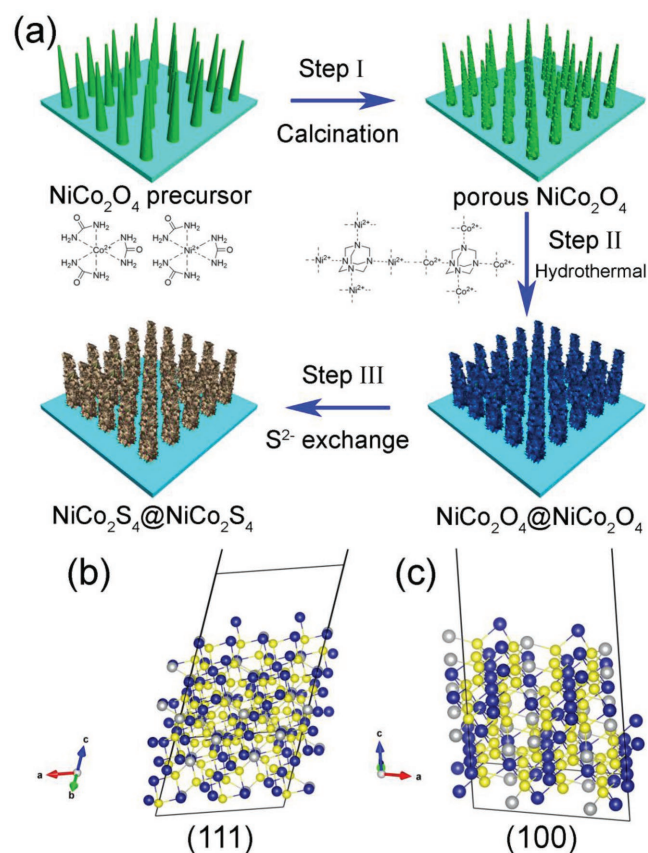


Figure 1. a) Schematic illustration showing the procedure to grow NiCo₂S₄@NiCo₂S₄ hierarchical nanostructures; b,c) (111) and (100) surface of the NiCo₂S₄, respectively. The gray, blue, and yellow balls represent nickel, cobalt, and sulfur atoms, respectively.

for diffusion-controlled approach. Compared to NiCo₂S₄ materials, NiCo₂O₄ counterparts present smaller lattice parameter, which may restrain the fast ion diffusion during electrochemical energy storage process.

The X-ray diffraction (XRD) patterns shown in Figure 2a correspond to the standard *Fd-3m* crystal structures of NiCo₂O₄ (JCPDS No.73-1702). NiCo₂O₄ arrays were coated on the Ni foam uniformly and with high density, as observed from the low-magnification scanning electron microscope (SEM) image in Figure 2b. High-magnification SEM images in Figure 2c,d show that the length of the NiCo₂O₄ nanorod was several micrometers and the width of which was ≈100 nm. The nanorods intersected with each other to form the dendritic structure. After the annealing process, porous structures were formed on the NiCo₂O₄ nanorod arrays surface, as indicated from the transmission electron microscopy (TEM) images, Figure 2e, which was due to gas evaporation during this process. Porous structures are of significant benefit for ion-transfer processes and contacting with the electrolyte. Figure 2f represents the high resolution transmission electron microscope (HRTEM) image of one part of the NiCo₂O₄ nanorod, the lattice fringes give an interplanar spacing of 0.165 nm, corresponding to the (422) lattice plane of *Fd-3m* phase of NiCo₂O₄ crystal. The top right corner inset corresponds to the fast Fourier transformation (FFT) diffraction pattern.

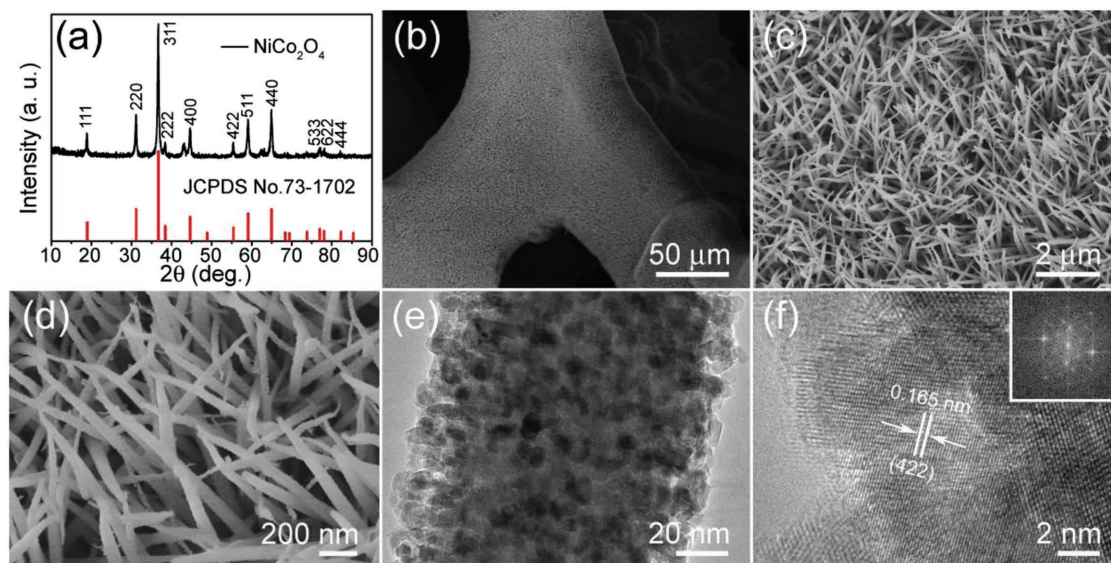


Figure 2. a) XRD pattern of the NiCo_2O_4 nanorod arrays, b–d) low to high magnification SEM images of the NiCo_2O_4 nanorod arrays, e) TEM image of a single NiCo_2O_4 nanorod, and f) lattice resolved HRTEM image of a NiCo_2O_4 nanorod, the inset showing its corresponding FFT pattern.

After another hydrothermal treatment to form the $\text{NiCo}_2\text{O}_4@ \text{NiCo}_2\text{O}_4$ hierarchical nanostructures, the uniform and high density of NiCo_2O_4 arrays were well preserved, as can be seen in low-magnification SEM image in **Figure 3a**. High-magnification SEM image (Figure 3b) and TEM image (Figure 3c) show the NiCo_2O_4 nanorods (branch structures) effectively and completely covered by the NiCo_2O_4 nanosheets (leaf structures), leading to a large volume of interspace inside these structures. The HRTEM of $\text{NiCo}_2\text{O}_4@ \text{NiCo}_2\text{O}_4$ core@shell heterostructures is shown in Figure 3d. The NiCo_2O_4 nanosheets have a d -spacing of 0.24 nm

corresponding to the (311) plane of NiCo_2O_4 , which agrees well with the obtained XRD results (Figure S2, Supporting Information). The corresponding FFT (top right corner inset) was taken from the HRTEM image of the nanosheet part of Figure 3d.

After S^{2-} exchange to form $\text{NiCo}_2\text{S}_4@ \text{NiCo}_2\text{S}_4$ hierarchical nanostructures, the dendritic structure was shown to remain intact with the NiCo_2S_4 nanosheets uniformly coated on the NiCo_2S_4 nanorods, as can be seen from SEM images (**Figure 4a–c**) and TEM images (Figure 4d). HRTEM of Figure 4e represents the junctions of the NiCo_2S_4 nanosheets and nanorods, the lattice planes of NiCo_2S_4 core-shell structures matched well with each other, thus facilitating strong binding. Figure 4f is an energy dispersive X-ray detector (EDX) spectrum recorded from the TEM images, the presence of Ni, Co, and S elements is in agreement with our expected products, the C, O, and Cu signals come from the TEM grid. Furthermore, the XRD pattern of $\text{NiCo}_2\text{S}_4@ \text{NiCo}_2\text{S}_4$ hierarchical nanostructures (Figure S3, Supporting Information) confirmed it corresponded to the standard $Fd-3m$ structures of NiCo_2S_4 (JCPDS No. 20-0782). By controlling the ligand environment, the orientation of the lattice plane can be tuned. As for the Ni foam substrate with the orientation of (111), the orientation of attached NiCo_2S_4 materials should be (111) to obtain the minimal coincident interface area (Database from materialsproject.org). Therefore, the stronger binding and less mismatched geometrical interface of the active materials and current collectors can be acquired. In this work, the well-designed synthetic procedure guaranteed the orientation of the nanorod with

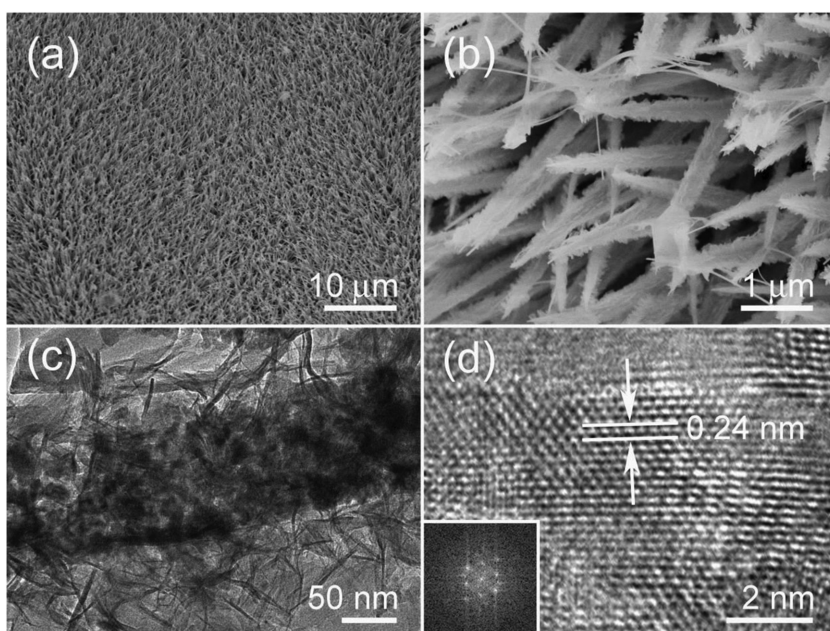


Figure 3. a,b) Low- and high-magnification SEM images of $\text{NiCo}_2\text{O}_4@ \text{NiCo}_2\text{O}_4$ hierarchical nanostructures, c) TEM image of a single $\text{NiCo}_2\text{O}_4@ \text{NiCo}_2\text{O}_4$ hierarchical nanostructure, d) HRTEM image of the NiCo_2O_4 nanosheet, the inset showing its corresponding FFT pattern.

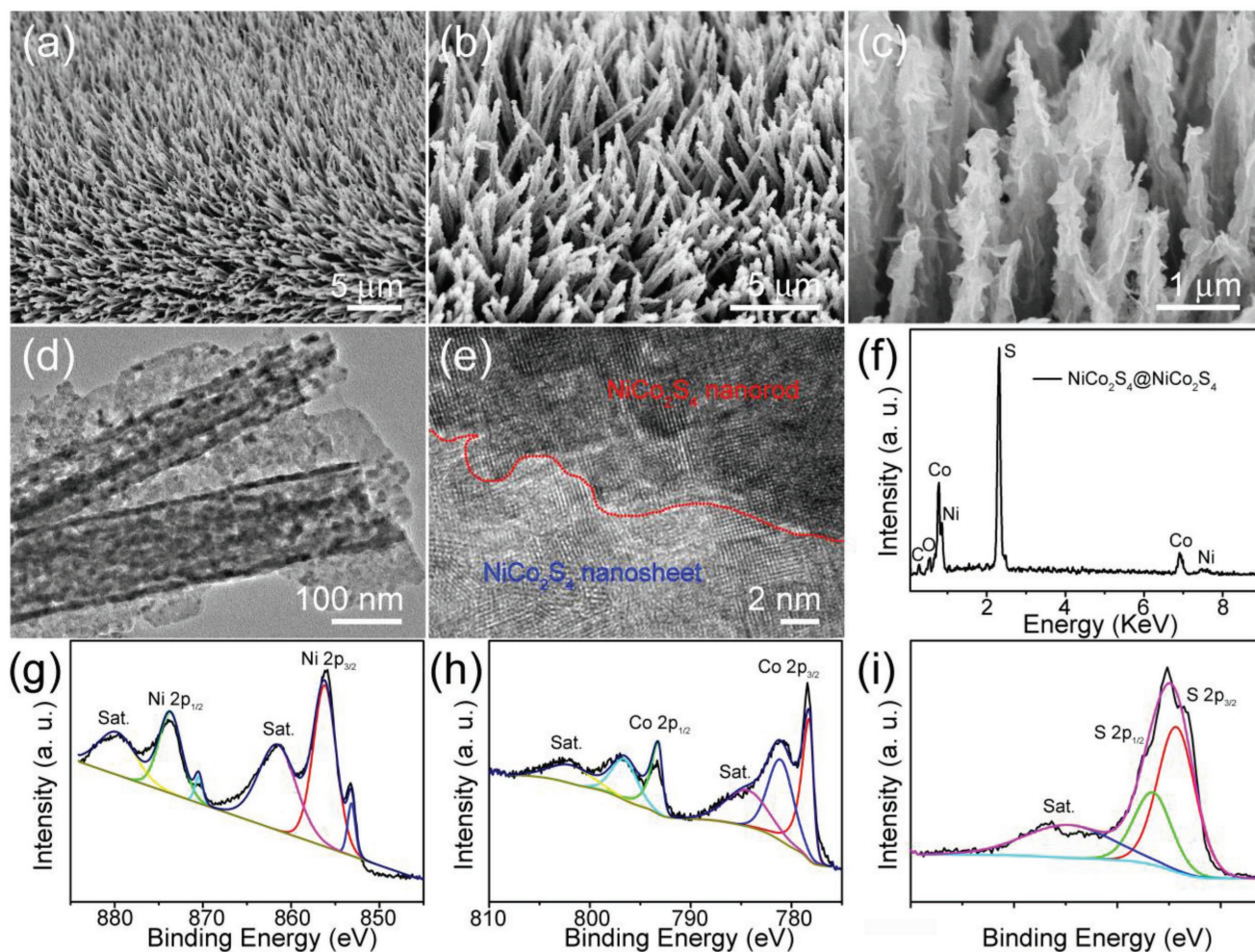


Figure 4. a–c) Low and enlarged SEM images of $\text{NiCo}_2\text{S}_4@/\text{NiCo}_2\text{S}_4$ hierarchical nanostructures, d,e) TEM and HRTEM images of the $\text{NiCo}_2\text{S}_4@/\text{NiCo}_2\text{S}_4$ hierarchical nanostructures. f) EDX pattern taken from such $\text{NiCo}_2\text{S}_4@/\text{NiCo}_2\text{S}_4$ hierarchical nanostructures. g–i) XPS survey scan of Ni2p, Co2p, and S2p regions, respectively.

exposed lattice plane of (111) in Figure S4 (Supporting Information), thus providing robust building blocks. Moreover, the nanosheets with other different orientation enlarged the surface area and formed 3D structures.

The presence of Ni, Co, and S elements can be confirmed by X-ray photoelectron spectroscopy (XPS) analysis results shown in Figure 4g–i. As illustrated in Figure 4g, the Ni 2p peak which reflects the chemical and electric states of the Ni atoms in the as-prepared samples has significantly split spin–orbit components ($\Delta\text{Ni} = 17.2$ eV). The intensive peaks centered at 870.5 and 853.3 eV are attributed to Ni 2p_{3/2} and Ni 2p_{1/2}, respectively, suggesting the appearance of the valence state of +2 for Ni. In addition, a multiplet–split Ni 2p_{3/2} peak (≈ 873.4 eV) and a multiplet–split Ni 2p_{1/2} peak (≈ 856.2 eV) are also presented in the XPS Ni 2p spectrum, showing the valence state of +3. Their corresponding satellite peaks are located at 606.6 and 625.0 eV, respectively. Figure 4h displays the Co 2p region of the XPS. Similar to Ni 2p, the Co 2p peaks also contains spin–orbit doublets ($\Delta\text{Co} = 15.0$ eV). The doublets consist of a lower (Co 2p_{3/2}) and a higher (Co 2p_{1/2}) energy band centered at 880.0

and 862.8 eV, respectively. Furthermore, two shake-up satellites of the Co 2p_{3/2} and Co 2p_{1/2} bands can be found in Figure 4h as well, which further proves the existence of Co content in the as-synthesized compound with the mixture of Co^{2+} and Co^{3+} . The S content in the $\text{NiCo}_2\text{S}_4@/\text{NiCo}_2\text{S}_4$ sample can also be confirmed by the XPS analysis whose results are illustrated in Figure 4i. The S 2p spectrum can be divided into two main peaks located at ≈ 162.0 and ≈ 163.2 eV as well as one shake-up satellite centered at ≈ 169.0 eV. The component at 163.2 eV corresponds to metal–sulfur bonds, and the peak at 162.0 eV can be attributed to sulfur ions at low coordination on the surface.^[17]

To demonstrate the electrochemical superiority of the $\text{NiCo}_2\text{S}_4@/\text{NiCo}_2\text{S}_4$ hierarchical heterostructures, we performed a comparative study with the counterpart $\text{NiCo}_2\text{O}_4@/\text{NiCo}_2\text{O}_4$ hierarchical heterostructures and NiCo_2O_4 nanorod arrays in a three-electrode configuration using 1.0 M KOH electrolyte. Figure 5a shows the cyclic voltammogram (CV) curves for $\text{NiCo}_2\text{S}_4@/\text{NiCo}_2\text{S}_4$ hierarchical nanostructures at different scan rates over a potential window of -0.20 – 0.60 V (vs saturated calomel electrode (SCE)). The CV curves display two pairs of redox

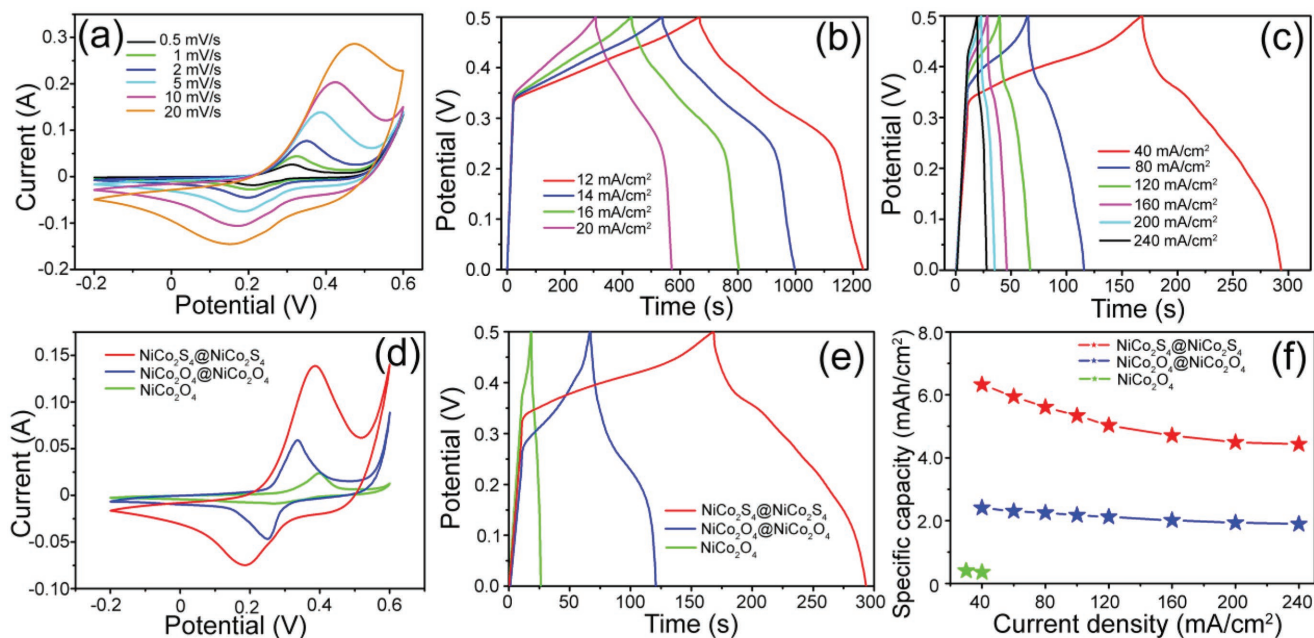
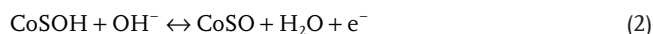


Figure 5. a) CV curves for NiCo₂S₄@NiCo₂S₄ hierarchical nanostructures at different scan rates. Galvanostatic charge–discharge curves for NiCo₂S₄@NiCo₂S₄ hierarchical nanostructures at b) low current densities from 12 to 20 mA cm⁻² and c) at high current densities from 40 to 240 mA cm⁻². d) CV curves for as-synthesized NiCo₂S₄@NiCo₂S₄, NiCo₂O₄@NiCo₂O₄ hierarchical nanostructures and NiCo₂O₄ nanorod arrays, recorded at a scan rate of 5 mV s⁻¹. e) Galvanostatic charge–discharge curves for as-synthesized NiCo₂S₄@NiCo₂S₄, NiCo₂O₄@NiCo₂O₄ hierarchical nanostructures and NiCo₂O₄ nanorod arrays, recorded at a current density of 40 mA cm⁻². f) A comparison of specific capacities for NiCo₂S₄@NiCo₂S₄, NiCo₂O₄@NiCo₂O₄ hierarchical heterostructures and NiCo₂O₄ nanorod arrays as a function of the current density at high current densities.

peaks, indicating the presence of redox reactions of NiCo₂S₄ during the electrochemical process. These distinct peaks might be attributed to the reversible Faradaic redox processes of Co²⁺/Co³⁺/Co⁴⁺ and Ni²⁺/Ni³⁺ redox couples based on the following reactions^[4,18]



With a 40-fold increase in the sweep rate, from 0.5 to 20 mV s⁻¹, the anodic peak current increases and the cathodic peak current density decreases, suggesting a relatively low resistance of the electrode and fast redox reactions at the interface of the electrode and electrolyte.^[19]

Figure 5b shows representative galvanostatic charge–discharge (GCD) curves of NiCo₂S₄@NiCo₂S₄ hierarchical heterostructures electrodes at low current densities of 12, 14, 16, and 20 mA cm⁻². Consistent with the CV results, the plateaus in the CD curves indicate the existence of Faradaic processes. These CD curves are approximately symmetric, indicating that NiCo₂S₄@NiCo₂S₄ hierarchical heterostructured electrodes have good electrochemical capacitive characteristics and superior reversible redox properties. The CD curves are still symmetrical even at a current density of 20 mA cm⁻², as indicated by the very high rate stability. The discharge areal capacitance performance was calculated from the GCD curves, NiCo₂S₄@NiCo₂S₄ hierarchical heterostructured electrodes exhibited

discharge areal-specific capacities of 8.20, 7.75, 7.18, and 6.37 mAh cm⁻² at 12, 14, 16, and 20 mA cm⁻² respectively, which is higher than the NiCo₂O₄@NiCo₂O₄ hierarchical nanostructures (4.58, 4.02, 3.73, 3.32, and 3.03 mAh cm⁻² at 6, 10, 12, 16, and 20 mA cm⁻², Figure S5e, Supporting Information) and NiCo₂O₄ nanorod arrays (1.30, 0.78, 0.63, 0.52, and 0.48 mAh cm⁻² at 2, 6, 10, 16, and 20 mA cm⁻², Figure S5b, Supporting Information).

To our surprise, NiCo₂S₄@NiCo₂S₄ hierarchical nanostructured electrodes can exhibit an outstanding areal-specific capacity even if the current densities increase from 40 to as high as 240 mA cm⁻². As shown in Figure 5c, the GCD curves are still approximate symmetrical even at such large current densities. According to the GCD curves, the discharge-specific capacities are 6.32, 5.61, 5.03, 4.71, 4.49, and 4.43 mAh cm⁻² at 40, 80, 120, 160, 200, and 240 mA cm⁻², respectively. To the best of our knowledge, this is the first time a report has been made that has such a high area capacity at so large a current density (Table S1, Supporting Information).

For comparison, the CV curves at a scan rate of 5 mV s⁻¹ of NiCo₂S₄@NiCo₂S₄, NiCo₂O₄@NiCo₂O₄ hierarchical nanostructures, and NiCo₂O₄ nanorod arrays electrodes are shown in Figure 5d. The detailed CV curves of NiCo₂O₄ nanorod arrays and NiCo₂O₄@NiCo₂O₄ hierarchical nanostructures are shown in Figure S5a,d (Supporting Information). Obviously, the CV integral area of NiCo₂S₄@NiCo₂S₄ hierarchical nanostructures electrode is larger than that of NiCo₂O₄@NiCo₂O₄ hierarchical nanostructures and the NiCo₂O₄ nanorod arrays electrodes, suggesting that the hierarchical heterostructures, especially NiCo₂S₄@NiCo₂S₄ architectures, have the largest specific

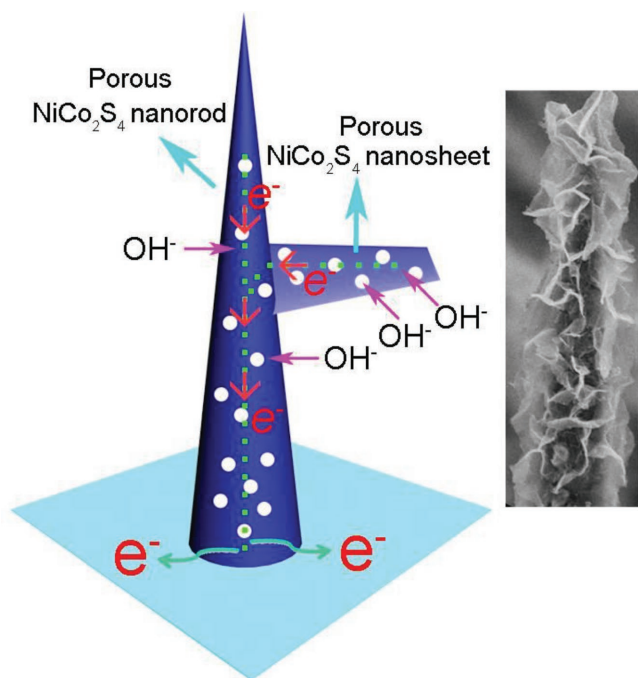


Figure 6. Schematic illustration of electron paths on porous NiCo₂S₄@NiCo₂S₄ nanostructures.

capacity. The comparison of GCD curves at a current density of 40 mA cm⁻² for the three electrodes is shown in Figure 5e. The areal-specific capacity of the NiCo₂S₄@NiCo₂S₄ hierarchical heterostructures is calculated to be 6.32 mAh cm⁻², which is more than twice that of the NiCo₂O₄@NiCo₂O₄ hierarchical heterostructures (2.40 mAh cm⁻²) and significantly larger than that of the NiCo₂O₄ nanorod arrays (0.36 mAh cm⁻²).

The rate capability is a critical parameter of electrochemical capacitors for assessing their application potential. Based on the charge–discharge curves of these materials, the summary plots of the areal-specific capacities versus the current densities are shown in Figure 5f. The discharge current density increases, the areal-specific capacities values decrease gradually for all systems. This can be explained by the diffusion-effect limiting the diffusion and migration of electrolyte ions OH⁻

within the electrode at a high discharge current density.^[20] It is worth noting that NiCo₂S₄@NiCo₂S₄ hierarchical nanostructures electrode achieve 4.43 mAh cm⁻² at 240 mA cm⁻² and hold 70.1% retention capacity when the rate increases from 40 to 240 mA cm⁻². Moreover, at lower current densities from 12 to 20 mA cm⁻² (Figure S6, Supporting Information), this electrode could keep 77.6% retention, implying a good rate capability. To our surprise, even though the areal-specific capacity of the NiCo₂O₄@NiCo₂O₄ hierarchical heterostructures electrode is much lower than NiCo₂S₄@NiCo₂S₄ hierarchical nanostructures electrode, when the rate increases from 40 to 240 mA cm⁻², it can still achieve a 78.3% retention, and at lower current densities from 6 to 20 mA cm⁻² (Figure S6, Supporting Information), it can even keep a 66% retention.

Such desirable electrochemical performance of NiCo₂S₄@NiCo₂S₄ might be attributed to their unique structural and compositional features, **Figure 6**. In particular, the void space in the interior together with the permeable thin walls provides sufficient electroactive sites and electrolyte–electrode interface for fast diffusion and reaction.^[21] In particular, the areal capacity of NiCo₂S₄@NiCo₂S₄ hierarchical nanostructures electrode is better than many reported in the literature (Table S1, Supporting Information).

To further understand the electrochemical performance characteristics, we resorted to electrochemical impedance spectroscopy (EIS) carried out in the frequency range of 100 kHz to 0.01 Hz. **Figure 7a** shows the Nyquist plots thus obtained. According to the order of decreasing frequency, the EIS spectra are composed of three distinct regions. First, the intercept on the real axis at the high frequency range provides the equivalent series resistance (R_s), which includes the inherent resistances of the electroactive material, bulk resistance of electrolyte, and contact resistance at the interface between electrolyte and electrode. Second, the charge transfer resistance (R_{ct}), which results from diffusion of electrons, can be calculated from the diameter of the semicircle in the high frequency range. Third, Warburg resistance, which describes the diffusion of redox species in the electrolyte, can be obtained from the slope of the EIS curve in the low frequency range. The vertical line at lower frequencies parallel to the imaginary axis indicates an ideal behavior, representative of the ion diffusion in the structure of the electrode.^[22] According to the recorded spectra **Figure 7a**, we have carried

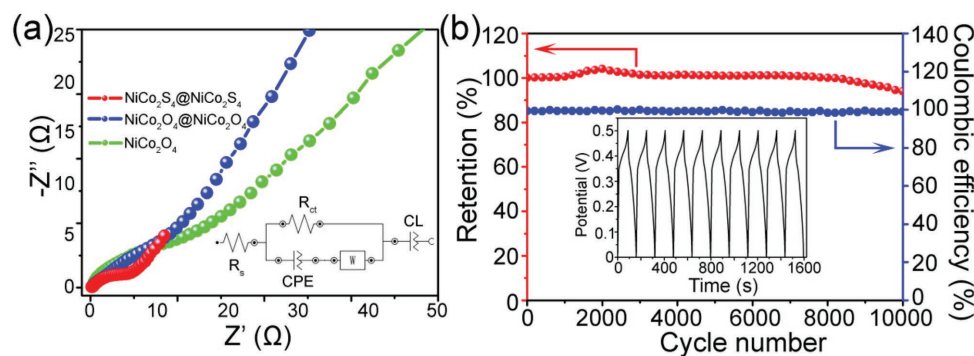


Figure 7. a) EIS spectra comparison of the NiCo₂S₄@NiCo₂S₄, NiCo₂O₄@NiCo₂O₄ hierarchical nanostructures, and NiCo₂O₄ nanorod arrays, the inset shows the equivalent fitting circuit of as-formed three electrodes. b) Cycle performance and Coulombic efficiency for the NiCo₂S₄@NiCo₂S₄ hierarchical nanostructures at a current of 60 mA cm⁻², inset shows the ten GCD curves measured after the 10 000 cycles.

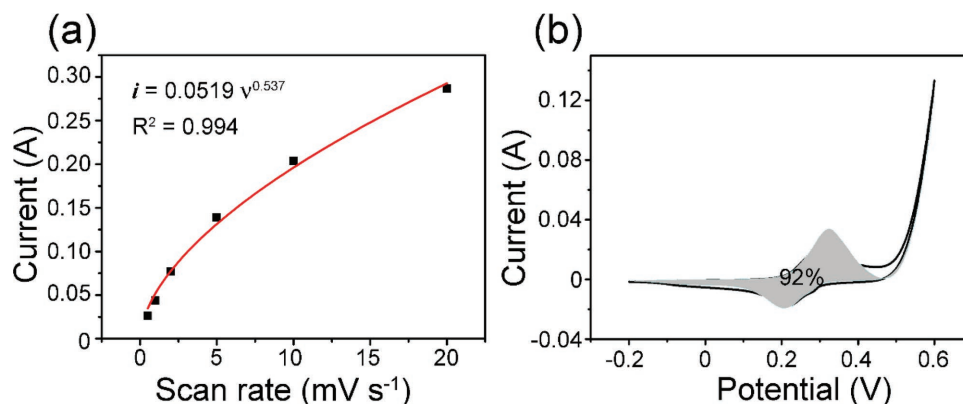


Figure 8. a) The anodic peak current against the scan rate of the NiCo₂S₄@NiCo₂S₄, b) Dunn method analysis of contribution from NiCo₂S₄@NiCo₂S₄. The gray region outlines the current contributed from diffusion controlled at the scan rate of 0.5 mV s⁻¹.

out the fitting process (Figure S7, Supporting Information), the insets in Figure 7a show the high frequency region of the spectra and the obtained equivalent fitting circuit, the values of Ohmic electrolyte resistance (R_s) obtained from the NiCo₂S₄@NiCo₂S₄ electrode is 0.028 Ω , lower than that of the NiCo₂O₄@NiCo₂O₄ (0.064 Ω) and NiCo₂O₄ electrode (0.214 Ω); and the charge transfer resistance (R_{ct}) values of NiCo₂S₄@NiCo₂S₄, NiCo₂O₄@NiCo₂O₄, and NiCo₂O₄ electrodes are 1.75, 3.20, and 4.85 Ω , respectively. The vertical line of NiCo₂S₄@NiCo₂S₄ hierarchical heterostructures at low frequencies is parallel to the imaginary axis, this reveals that NiCo₂S₄ has much higher electric conductivity in accord with results report elsewhere.^[12,23] Moreover, the as-calculated diffusion coefficients of OH⁻ are shown in Figure S8 and Table S2 (Supporting Information). To recap, the results clearly demonstrate that the NiCo₂S₄@NiCo₂S₄ hierarchical heterostructures display favorable charge-transfer kinetics and fast electron transport and thus exhibit dramatically enhanced pseudocapacitive performance.

Cycle stability is another key parameter in relation to the electrochemical performance of a RAB and was investigated at a current density of 60 mA cm⁻² for 10 000 GCD tests, as shown in Figure 7b. It was found that the NiCo₂S₄@NiCo₂S₄ hierarchical heterostructures electrode gained a capacitance increase over the first 2000 cycles (\approx 104% of the initial value), which could be ascribed to an activation process that occurred at the beginning of the test,^[24] the electrode is quite stable and \approx 93% of the specific capacity can still be retained after 10 000 cycles. The structure and morphology after the long cycling test and the structural evolution process are shown in Figure S9 (Supporting Information). The SEM image shows the NiCo₂S₄@NiCo₂S₄ hierarchical nanostructures after cycling test clearly stack together, and it can be found that the surface became relatively rough and loose. The electrode material undergoes gradual corrosion during long-term cycling. Based on the above analysis, the reaction mechanism can be proposed. As illustrated in inset of Figure S9a (Supporting Information), the surface of NiCo₂S₄ nanosheets is constantly corroded during repeated charge and discharge tests, resulting in an ultraloose structure and stack together. XRD test is also used to measure the crystal phase of the hierarchical nanostructures, as shown in Figure S9b (Supporting Information).

The diffraction peaks show a similar XRD pattern to the NiCo₂S₄ (JCPDS card No. 20-0782), indicating the NiCo₂S₄ phase still can be maintained even after long cycling tests. TEM images in Figure S9c (Supporting Information) further demonstrated the coarse surfaces and incompact structures, the dissolution of active materials and formation of oxides thin layers can be detected from HRTEM in Figure S9d (Supporting Information). Also, the electrode shows a high electrochemical reversibility with nearly 100% Coulombic efficiency maintained. The inset of Figure 7b shows the additional ten charging and discharging curves after 10 000 cycles at a current density of 60 mA cm⁻², and the Coulombic efficiency is about 99% for each cycle even after these long-term cycling tests.

To further illustrate the electrochemical reaction mechanism, according to Dunn's method, the relationship of anodic peaks at different scan rates and differentiation of the charge storage mechanism were separated. If the electrochemical redox reaction is performed as in a battery type, the peak current I varies as $V^{1/2}$; moreover, it varies as V for a capacitive process. For our designed dendritic electrodes, the index of 0.537 can be calculated from the CV curves at a scan rate from 0.5 to 20 mV s⁻¹, **Figure 8a**, thus indicating the semiinfinite diffusion control reaction for those materials. **Figure 8b** presents the details of the separated diffusion-limited process and capacitive process for the CV curve at a scan rate of 0.5 mV s⁻¹. About 92% of the capacity can be attributed to a battery-type contribution. With the increase of the scan rate, it is reasonable to see this value decreases to 43% at 20 mV s⁻¹ (Figure S10, Supporting Information), indicating the surface redox reaction processes is dominating at high scan rate.

A hybrid RAB was assembled with the NiCo₂S₄@NiCo₂S₄ hierarchical heterostructures on Ni foam as the cathode, activated carbon (AC) electrode as the anode (CV and kinetic analysis for active carbon in Figure S11, Supporting Information) to further evaluate the application potential of as-synthesized NiCo₂S₄@NiCo₂S₄ on Ni foam. **Figure 9a** shows the CV curves of the RAB at different scan rates ranging from 2 to 50 mV s⁻¹ in the voltage range of 0–1.6 V. Clearly, the CV curves showed hybrid capacity of both an electric double-layer capacitor and a redox reaction of a battery. Based on the GCD curves

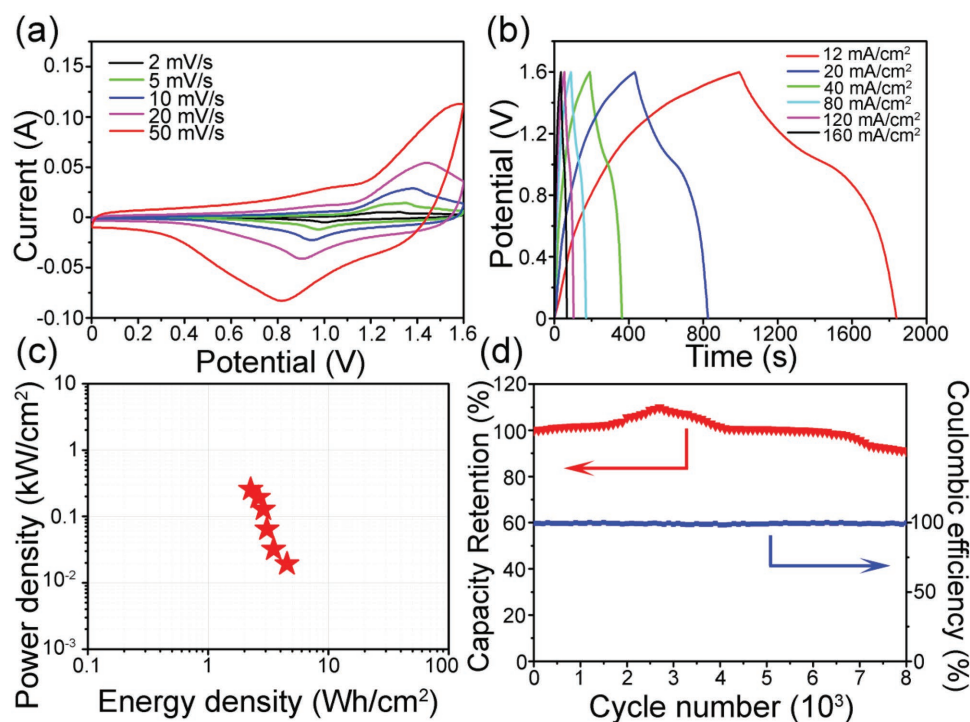


Figure 9. a) CV curves for the hybrid RABs (AC//NiCo₂S₄@NiCo₂S₄) at different scan rates; b) GCD curves of the hybrid RABs at different current density; c) Ragone plot of the hybrid RABs; and d) cycling performance of the devices.

at different current densities in Figure 9b, the RAB possessed the specific capacities of 3.53, 2.74, 2.41, 2.25, 2.04, and 1.76 mAh cm⁻² at current densities of 12, 20, 40, 80, 120, and 160 mA cm⁻². Thus, with a 13.3-time increase in the current density, the specific capacity is still retained, corresponding to 49.9% of the specific capacity retention (Figure S12, Supporting Information). Energy density and power density are two key metrics for evaluating the performances of energy storage devices. Figure 9c shows the plots of power density versus energy density (Ragone plot) of the hybrid RAB. The device exhibited a high area power density (maximum output value) of 0.26 kW cm⁻² and high area energy density (maximum output value) of 4.52 Wh cm⁻². In addition, The long-term cycling stability for the hybrid RAB was also tested by repeated charge and discharge measurements at a constant current density of 40 mA cm⁻². As shown in Figure 9d, after 8000 cycles, the hybrid RAB still retains 90% of the specific capacity, the Coulombic efficiency of the hybrid RAB stayed ≈100%, demonstrating the superior performance of as-assembled hybrid RAB.

The above results reveal NiCo₂S₄@ NiCo₂S₄ core/shell nanorods exhibit high-specific capacity as electrodes for batteries, excellent rate capability as well as remarkable cycling performance when used as an alkaline battery. Such excellent electrochemical performance is mainly attributed to the following factors. First, the void space between the ravine-like nanosheet structure effectively creates a spatial confinement for the electrolyte between the NiCo₂S₄ core and the NiCo₂S₄ shell. Within this open space, close contact is achieved between active materials allowing for facile electrolyte diffusion and

rapid ion transport. The open space in the hierarchical structure can serve as an “ion and electrolyte reservoir” to facilitate the transportation of electrolyte ions and can also buffer the volume change during charge/discharge process to protect the core materials. Second, the specific surface area of the hybrids is greatly increased due to the uniform hierarchical nanostructure. It is reported that a conformal coating of shell material can increase the surface area several times. The high-specific surface area can provide considerable electric double-layer capacitance.^[25] Third, due to the uniform connection between NiCo₂S₄ shell with the NiCo₂S₄ core, the physical charge on NiCo₂S₄ core can be transported eventually to the NiCo₂S₄ shell.

3. Conclusions

In conclusion, uniform NiCo₂S₄@NiCo₂S₄ hierarchical nanostructures were successfully fabricated by a three-step continuous hydrothermal route. The possible growth mechanisms were presented. The electrochemical investigation showed that the NiCo₂S₄@NiCo₂S₄ hierarchical nanostructures delivered a high discharge-specific capacity of 4.43 mAh cm⁻² even at a high current density of 240 mA cm⁻² as an electrode in RABs. Moreover, the as-designed electrodes presented excellent rate performance and high stability. The excellent electrochemical properties can be attributed to the advanced design of hierarchical microstructure with a highly porous structure that promoted ion transportation during the charge/discharge process. Detailed kinetic analysis presented the distribution of the

diffusion and surface controlled redox reactions in this energy storage systems. The work also delivered the design concept for hierarchical nanostructures as electrodes for RABs.

4. Experimental Section

Preparation of NiCo₂O₄ Nanoarrays on Ni Foam: The Ni foam was purchased from Kunshan Jiayisheng Electronics Co., Ltd with the thickness of ≈1 mm. The NiCo₂O₄ nanoarrays were synthesized on Ni foam (1 cm x 4 cm) using a one-step hydrothermal reaction followed by a simple postannealing process. All commercially available chemicals were used as received from Sinopharm Chemical Reagent Co. (Shanghai, China) without further purification. First, a piece of Ni foam (≈4 cm x 1 cm) was carefully cleaned with 5 M HCl solution in an ultrasound bath for 20 min to remove NiO layer on the surface and then rinsed with deionized water and absolute ethanol for several times until neutral. Then, in a typical synthesis, 0.675 g of NiCl₂·6H₂O, 1.185 g of CoCl₂·6H₂O, and 0.45 g urea were dissolved in 40 mL of H₂O at room temperature to form a clear pink solution and transferred into a 60 mL Teflon autoclave. After that, the treated Ni foam substrates were put into the Teflon autoclave. The Teflon lined autoclave was sealed and maintained at 140 °C for 8 h and then naturally cooled down to room temperature. The Ni foam with products was taken out from the autoclave and cleaned by ultrasonication in deionized water to remove the loosely attached products on its surface. Finally, the Ni foam substrate with loaded products was dried at 60 °C. In order to get crystallized NiCo₂O₄ nanoarrays on the Ni foam, the samples were then annealed at 300 °C in air for 2 h with a heating rate of 0.5 °C min⁻¹.

Preparation of NiCo₂O₄@NiCo₂O₄ Hierarchical Nanoarrays: In a typical synthesis, 0.34 g of Ni(NO₃)₂·6H₂O, 0.17 g of Co(NO₃)₂·6H₂O, and 0.24 g HMT were dissolved in a mixed solution contain 30 mL H₂O and 15 mL absolute ethanol at room temperature to form a clear solution and transferred into a 60 mL Teflon autoclave. After that, the prepared NiCo₂O₄ nanoarrays were put into the Teflon autoclave. It was then sealed and maintained at 150 °C for 8 h and allowed to naturally cool to room temperature. The Ni foam with products was taken out from the autoclave and cleaned by ultrasonication in deionized water to remove the loosely attached products on its surface. Finally, the Ni foam substrate with loaded products was dried at 60 °C. In order to get crystallized NiCo₂O₄@NiCo₂O₄ nanoarrays on Ni foam, the samples were annealed at 300 °C in air for 2 h with a heating rate of 0.5 °C min⁻¹.

Preparation of NiCo₂S₄@NiCo₂S₄ Hierarchical Nanoarrays: A piece of prepared NiCo₂O₄@NiCo₂O₄ hierarchical nanoarrays on Ni foam was soaked in a 40 mL solution containing 1 g of Na₂S in a 60 mL autoclave. After being sealed, the autoclave was heated at 90 °C for 24 h. The sample was opened and cooled to room temperature. The converted sample washed with distilled water and dried at 60 °C under vacuum.

Supporting Information

Supporting Information is available from the Wiley Online Library or from the author.

Acknowledgements

This work was financially supported by the National Natural Science Foundation of China (Grant Nos. 51602193, 51741203, 21601122 and 51672044), the Shanghai "Chen Guang" project (16CG63), the Program for Innovative Research Team in University of Ministry of Education of China (IRT_16R13), and the Fundamental Research Funds for the Central Universities, the Talent Program of Shanghai University of Engineering

Science, the China Scholarship Council/University College London for the Joint PhD scholarship program and EPSRC Centre for Doctoral Training in Molecular Modelling and Materials Science (EP/L015862/1).

Conflict of Interest

The authors declare no conflict of interest.

Keywords

dendritic nanostructures, kinetic analysis, nickel cobalt sulfides, rechargeable alkaline batteries

Received: October 13, 2017

Revised: March 7, 2018

Published online:

- [1] a) P. Simon, Y. Gogotsi, *Nat. Mater.* **2008**, *7*, 845; b) M. F. El-Kady, Y. L. Shao, R. B. Kaner, *Nat. Rev. Mater.* **2016**, *1*, 16033; c) M. Matsusaki, H. Ajiro, T. Kida, T. Serizawa, M. Akashi, *Adv. Mater.* **2012**, *24*, 454; d) P. Huang, C. Lethien, S. Pinaud, K. Brousse, R. Laloo, V. Turq, M. Respaud, A. Demortière, B. Daffos, P. L. Taberna, B. Chaudret, Y. Gogotsi, P. Simon, *Science* **2016**, *351*, 6274.
- [2] a) V. Augustyn, P. Simon, B. Dunn, *Energy Environ. Sci.* **2014**, *7*, 1597; b) H. Sun, G. Xin, T. Hu, M. Yu, D. Shao, X. Sun, J. Lian, *Nat. Commun.* **2014**, *5*, 4526.
- [3] a) H. Jiang, C. Li, T. Sun, J. Ma, *Nanoscale* **2012**, *4*, 807; b) S. Boukhalifa, K. Evanoff, G. Yushin, *Energy Environ. Sci.* **2012**, *5*, 6872.
- [4] J. Pu, F. Cui, S. Chu, T. Wang, E. Sheng, Z. Wang, *ACS Sustainable Chem. Eng.* **2014**, *2*, 809.
- [5] a) G. He, X. Han, R. Zou, T. Zhao, Z. Weng, S. H. Kimura, Y. Lu, H. L. Wang, Z. X. Guo, I. P. Parkin, *Adv. Funct. Mater.* **2017**, *27*, 1604903. b) G. He, M. Qiao, W. Li, Y. Lu, T. Zhao, R. Zou, B. Li, J. A. Darr, J. Hu, M. M. Titirici, I. P. Parkin, *Adv. Sci.* **2017**, *4*, 1600214.
- [6] a) Q. Liu, Z. Wu, Z. Ma, S. Dou, J. Wu, L. Tao, X. Wang, C. Ouyang, A. Shen, S. Wang, *Electrochim. Acta* **2015**, *177*, 298; b) Q. Liu, J. Jin, J. Zhang, *ACS Appl. Mater. Interfaces* **2013**, *5*, 5002; c) H. Huo, Y. Zhao, C. Xu, *J. Mater. Chem. A* **2014**, *2*, 15111.
- [7] a) H. Ma, J. He, D. Xiong, J. Wu, Q. Li, V. Dravid, Y. Zhao, *ACS Appl. Mater. Interfaces* **2016**, *8*, 1992; b) M. Sun, J. Tie, G. Cheng, T. Lin, S. Peng, F. Deng, F. Ye, L. Yu, *J. Mater. Chem. A* **2015**, *3*, 1730; c) W. Kong, C. Lu, W. Zhang, J. Pu, Z. Wang, *J. Mater. Chem. A* **2015**, *3*, 12452.
- [8] a) S. Peng, L. Li, C. Li, H. Tan, R. Cai, H. Yu, S. Mhaisalkar, M. Srinivasan, S. Ramakrishna, Q. Yan, *Chem. Commun.* **2013**, *49*, 10178; b) M. L. Yan, Y. D. Yao, J. Q. Wen, L. Long, M. L. Kong, G. G. Zhang, X. M. Liao, G. F. Yin, Z. B. Huang, *ACS Appl. Mater. Interfaces* **2016**, *8*, 24525.
- [9] L. Hou, Y. Shi, S. Zhu, M. Rehan, G. Pang, X. Zhang, C. Yuan, *J. Mater. Chem. A* **2017**, *5*, 133.
- [10] L. Shen, L. Yu, H. B. Wu, X. Y. Yu, X. Zhang, X. W. Lou, *Nat. Commun.* **2015**, *6*, 6694.
- [11] R. Zou, K. Xu, T. Wang, G. He, Q. Liu, X. Liu, Z. Zhang, J. Hu, *J. Mater. Chem. A* **2013**, *1*, 8560.
- [12] H. Chen, J. Jiang, L. Zhang, H. Wan, T. Qi, D. Xia, *Nanoscale* **2013**, *5*, 8879.

- [13] G. He, M. Ling, X. Han, D. I. Abou El Amaiem, Y. Shao, Y. Li, W. Li, S. Ji, B. Li, Y. Lu, R. Zou, F. Ryan Wang, D. J. L. Brett, Z. Xiao Guo, C. Blackman, I. P. Parkin, *Energy Storage Mater.* **2017**, *9*, 119.
- [14] J. Xiao, L. Wan, S. Yang, F. Xiao, S. Wang, *Nano Lett.* **2014**, *14*, 831.
- [15] C. W. Kung, H. W. Chen, C. Y. Lin, K. C. Huang, R. Vittal, K. C. Ho, *ACS Nano* **2012**, *6*, 7016.
- [16] R. Zou, M. F. Yuen, L. Yu, J. Hu, C. S. Lee, W. Zhang, *Sci. Rep.* **2016**, *6*, 20264.
- [17] H. C. Chen, S. Chen, H. Y. Shao, C. Li, M. Q. Fan, D. Chen, G. L. Tian, K. Y. Shu, *Chem. - Asian J.* **2016**, *11*, 248.
- [18] H. Wan, J. Jiang, J. Yu, K. Xu, L. Miao, L. Zhang, H. Chen, Y. Ruan, *CrystEngComm* **2013**, *15*, 7649.
- [19] C. Yuan, J. Li, L. Hou, X. Zhang, L. Shen, X. W. D. Lou, *Adv. Funct. Mater.* **2012**, *22*, 4592.
- [20] H. Jiang, T. Zhao, C. Li, J. Ma, *J. Mater. Chem.* **2011**, *21*, 3818.
- [21] C. Yuan, H. B. Wu, Y. Xie, X. W. D. Lou, *Angew. Chem., Int. Ed.* **2014**, *53*, 1488.
- [22] R. B. Rakhi, W. Chen, D. Cha, H. N. Alshareef, *Nano Lett.* **2012**, *12*, 2559.
- [23] J. Xiao, X. Zeng, W. Chen, F. Xiao, S. Wang, *Chem. Commun.* **2013**, *49*, 11734.
- [24] W. Li, G. Li, J. Sun, R. Zou, K. Xu, Y. Sun, Z. Chen, J. Yang, J. Hu, *Nanoscale* **2013**, *5*, 2901.
- [25] J. Wang, D. Chao, J. Liu, L. Li, L. Lai, J. Lin, Z. Shen, *Nano Energy* **2014**, *7*, 151.